

Magnetic order and transport in a spin-fermion model on a superlattice

Sabyasachi Tarat,¹ Jian Li,¹ Richard T. Scalettar,² and Rubem Mondaini¹

¹*Beijing Computational Science Research Center, Beijing 100193, China*

²*Department of Physics, University of California, Davis, California 95616, USA*

We consider a spin-fermion model consisting of free electrons coupled to classical spins, where the latter are embedded in a quasi one-dimensional superlattice structure consisting of spin blocks separated by spinless buffers. Using a spiral ansatz for the spins, we study the effect of the electron mediated Ruderman-Kittel-Kasuya-Yosida (RKKY) interaction on the $T = 0$ ground state of the system. We find that the RKKY interaction can lead to ferromagnetic, antiferromagnetic, or intermediate spiral phases for different system parameters. When the width is much larger than the length of the individual blocks, the spiral phases are suppressed, and the ground state oscillates between ferromagnetic and antiferromagnetic order as the size of the buffer regions is varied. This is accompanied by a corresponding oscillation in the Drude weight reflecting an increased conductivity in the ferromagnetic state compared to the antiferromagnetic one. These results are reminiscent of classic giant magnetoresistance phenomena observed in a similar geometry of thin, sandwiched magnetic and non-magnetic layers. Our analysis provides a robust framework for understanding the role of the RKKY interaction on the ground state order and corresponding transport properties of such systems, extending beyond the conventional perturbative regime.

I. INTRODUCTION

Spin-fermion models, consisting of localized degrees of freedom (the ‘spins’) interacting with itinerant degrees of freedom (the ‘fermions’), have proven useful in capturing the essential physics of many correlated systems in condensed matter physics, including manganites [1], cuprates [2, 3], nickelates [4, 5], iron superconductors [6–8], heavy fermion materials [9, 10], and ferromagnetic semiconductors [11–14], among others. In these materials, there is often a natural separation of localized and itinerant electrons, such as the localized t_{2g} and mobile e_g electrons in manganites [15], or the localized $3d^5$ electrons, which form a spin $5/2$, and the mobile Mo electrons, in the double perovskite $\text{Sr}_2\text{FeMoO}_6$ [16–18]. In many such cases, the former have large local moments, and may be approximated as classical spins, resulting in a simplified model of itinerant electrons coupled to classical Heisenberg spins. The simplest example of this is the double exchange model [19, 20], which has been applied to study the phenomenon of colossal magnetoresistance [15] and, under different contexts, the emergence of Majorana edge states for magnetic chains in contact with an s -wave superconductor [21–24].

An important ingredient driving the physics in such models is the effective Ruderman-Kittel-Kasuya-Yosida (RKKY) interaction [25–27] between the spins mediated by the mobile conduction electrons [28]. When an isolated impurity is inserted in a sea of electrons, it polarizes the electron sea around it, which can act on another impurity, resulting in an indirect long range spin-spin interaction that decays as $1/r^d$ in d dimensions, and oscillates in sign with a period determined by the Fermi vector k_F . In a lattice of spins, the resultant interactions lead to a variety of spiral (SP), ferromagnetic (FM) and antiferromagnetic (AF) phases, generating a very rich phase diagram [29–32].

An intriguing situation is created when the spins

are embedded in a superlattice structure with spinless ‘buffer’ regions separating ‘blocks’ of spins (See Fig. 1). This geometry is realized, for example, in the classic giant magnetoresistance (GMR) experiments consisting of alternating thin layers of FM and non-magnetic (NM) material sandwiched together [33–36]. In such a setup, the simple two-spin RKKY interaction is generalized to a more complex effective one between the spin blocks, with the NM buffer regions playing the role of the spin-spin separation. By adjusting the length of these buffer regions, the FM ‘blocks’ may be aligned antiferromagnetically with respect to each other. When a magnetic field is applied, a huge increase in conductivity is observed, lending the phenomenon its name. The conventional explanation follows from different scattering amplitudes for up and down spin electrons, leading to a much smaller resistance when the magnetic field aligns all moments in the different blocks in the same direction [35, 36]. The detailed spatial character of the RKKY interaction is crucial in determining the physics of the system.

Several existing papers have generalized the theory of the RKKY interaction to larger magnetic clusters [37], or explored experimentally the nature of magnetic order for small clusters [38] rather than single magnetic impurities. The theoretical work has not, however, linked these more complex forms of the conduction-electron-mediated interaction to the transport properties, a link which is crucial to modeling GMR phenomena. Moreover, much of this work has been confined to the perturbative RKKY regime, which fails to capture the subtle interplay of strong spin polarization and finite size effects of the magnetic clusters on the ground state, and especially, the transport properties.

Here, we address this outstanding issue by studying the role of the RKKY interaction on the ground state order and corresponding transport properties in a superlattice system. Using a spiral ansatz for the classical spins, we analyse a spin fermion model and investigate

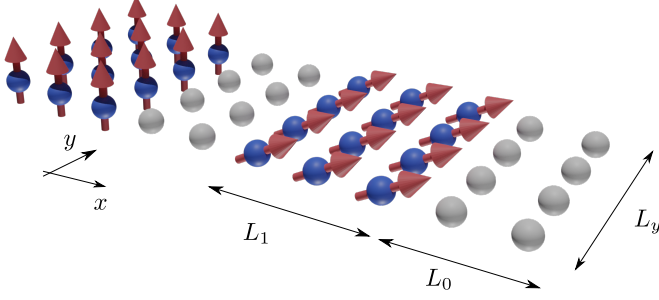


FIG. 1. The superlattice geometry. The blue spheres represent lattice sites in the spin blocks of length L_1 possessing classical Heisenberg spins \vec{S}_i (represented by the red vectors), while the white spheres represent the intermediate buffer sites without spins. The combined spin and buffer block, of length $L_c = L_0 + L_1$, and width L_y , is repeated in the x -direction N_c times. PBC are imposed in both the x and y directions.

the possible ground states at $T = 0$ in various parameter regimes, going far beyond the standard perturbative RKKY regime. We show that, in general, the RKKY interaction can lead to FM, SP and AF order for different parameter values. As the transverse width is increased, however, the SP phases are suppressed. In this regime, we find that the ground state oscillates between FM and AF order as the buffer length is varied. The Drude weight D shows corresponding oscillations as well, demonstrating enhanced conductivity in the FM state, in agreement with observations from GMR experiments [39, 40]. We summarize these results in a series of phase diagrams in the buffer length L_0 and Hund's coupling J_H plane for different values of the chemical potential μ . Analysis of these oscillations shows that, somewhat surprisingly, their salient characteristics, such as the dependence of their periods on μ , can be explained from simple considerations of standard RKKY theory even when the system is far away from the perturbative regime. On the other hand, transport properties like the spin resolved Drude weight display unexpected results that cannot be derived from the perturbative picture, underscoring the ability of our calculations to capture effects beyond such conventional methods. Finally, we discuss the implications of these results, expand on their connection to the GMR experiments, and conclude by outlining possible extensions in future work.

II. MODEL AND METHODS

We focus on studying the effect of the RKKY interaction on the spins in a superlattice geometry, inspired by the classic experiments on GMR [33–36]. We consider a quasi one-dimensional (1D) lattice with length L_x and width L_y , where the classical spins reside on blocks of length L_1 , alternating with spinless buffer blocks of

length L_0 . This unit of length $L_c = L_0 + L_1$ is repeated N_c times in the x -direction, and thus $L_x = N_c L_c$, and the total number of lattice points $L_t = L_x L_y$. We impose periodic boundary conditions (PBC) along both the x and y directions. Figure 1 shows the geometric layout in detail.

In real materials, electron-spin and spin-spin couplings usually originate from a variety of physical phenomena involving multiple orbitals [41]. However, our concern here will be to construct the simplest possible model that describes our system, i.e., FM blocks in a superlattice. Hence, our model parameters should be interpreted as phenomenological, effective variables and not material specific ones. To begin with, we model the localized moments by classical Heisenberg spins \vec{S}_i , which are coupled to the itinerant electrons by a ferromagnetic Hund's coupling J_H . We include a nearest neighbour ($\langle \dots \rangle$) ferromagnetic spin-spin coupling of strength J_F to induce ferromagnetic order inside each spin block, mimicking the ferromagnetic layers in the GMR experiments. The itinerant electrons are characterised by a nearest neighbour hopping t and a chemical potential μ . For simplicity, we assume that the hopping elements are the same in the spin and buffer blocks. Thus, our Hamiltonian is given by,

$$\mathcal{H} = (-t) \sum_{\langle ij \rangle \sigma} (c_{i\sigma}^\dagger c_{j\sigma} + \text{h.c.}) - \mu \sum_{i\sigma} c_{i\sigma}^\dagger c_{i\sigma} - J_H \sum_{i\alpha\beta} \vec{S}_i \cdot c_{i\alpha}^\dagger \vec{\sigma}_{\alpha\beta} c_{i\beta} - J_F \sum_{\langle ij \rangle} \vec{S}_i \cdot \vec{S}_j, \quad (1)$$

where $c_{i\sigma}^\dagger$ ($c_{i\sigma}$) denotes the fermionic creation (annihilation) operator at site i with spin σ , and $\vec{\sigma} = (\sigma^x, \sigma^y, \sigma^z)$ is the vector of spin-1/2 Pauli matrices. The classical spins \vec{S}_i in the second line, as explained before, refer to the localized moments in the ferromagnetic region, and are absent in the buffers. We will further assume that the ratio J_F/J_H is large enough so that all spins within a particular block are aligned ferromagnetically at $T = 0$, as seen in experiments. We reiterate that the final term, $J_F \vec{S}_i \cdot \vec{S}_j$, is a purely phenomenological intra-block term which acts only on the classical spins \vec{S}_i to ensure a totally ferromagnetic orientation inside each block; the interactions between the itinerant electrons and the spins are entirely encapsulated by the Hund's coupling term with strength J_H . With the above assumptions, we will drop this term from subsequent calculations.

Without the J_F term, our Hamiltonian is determined by J_H/t and μ/t . Keeping μ constant, the two extreme limits of the model are given by $J_H/t = 0$ and $J_H/t = \infty$. The former limit corresponds to ferromagnetic blocks that are uncoupled to free electrons on the superlattice. When J_H is turned on, a perturbative expansion can be performed, leading to the standard RKKY expression (see Appendix A). The other limit, $J_H/t = \infty$, corresponds to a situation where the electrons are localized, leaving individual spins uncorrelated (other than implicitly through the large intra-block J_F in our model). In

a normal lattice, a small non-zero t leads to the well known spinless double exchange model [42], with an effective hopping that favours FM order. In our superlattice setup, we also expect a finite t to lead to FM order among the spin blocks, but with a reduced magnitude $\sim t^2/J_H$ due to the energy mismatch between the electronic states at the spin block boundary as a result of the polarization by J_H . When $t \sim J_H$, the effects of hopping and spin polarization are of the same order of magnitude, and a simplified solution to the problem is no longer possible.

Our Hamiltonian obeys particle-hole symmetry at $\mu = 0$ (see Appendix C), which implies that the number density is strictly fixed at $\langle n \rangle = 1$ for all parameter values at this point. Away from this special value, $\langle n \rangle$ could vary in principle with the parameters, especially the buffer length L_0 . In practice, however, we find that $\langle n \rangle$ saturates with L_0 fairly quickly over a large range of μ (See Appendix D). Furthermore, in a typical experimental setup, μ can be controlled by adjusting the gate voltage. In view of this, our calculations will be done at fixed μ instead of $\langle n \rangle$.

Since this Hamiltonian is quadratic in the fermions, it can be solved by diagonalizing a matrix of size $2L_t \times 2L_t$ for any arbitrary configuration of the spins $\{\tilde{S}_i\}$. The doubling occurs due to mixing of the electron spins by the Hund's coupling term. However, as our spins are distributed on a periodic superlattice geometry, the ground state at $T = 0$ is expected to be regular, and not random. It is well known that in a regular lattice geometry, with spins on each site, the competition between the Fermi wave vector k_F and J_H leads to a variety of spiral spin configurations at different fillings in 1D [29–31]. Motivated by these results, we assume a similar spiral ansatz for our quasi 1D superlattice system. The width L_y provides an added ingredient in our system due to the presence of multiple transverse modes.

Following the reasoning in Refs. [21, 22, 29], we argue that in the absence of spin orbit coupling (leading to antisymmetric spin-spin interactions such as the Dzyaloshinskii-Moriya coupling [43, 44]), at zero external magnetic field, a planar ground state ansatz results, in no loss of generality. Hence, we assume a spiral state of the following form:

$$\begin{aligned} \mathcal{S}_x^m &= \cos(qx_m) \\ \mathcal{S}_y^m &= \sin(qx_m) \\ \mathcal{S}_z^m &= 0. \end{aligned} \quad (2)$$

Here, \mathcal{S}^m denotes any of the local spins in the ‘block’ m , x_m denotes the ‘block’ coordinate, and $q = 2\pi n/N_c$ ($n = 0, \dots, N_c - 1$), denotes a ‘block’ momentum index. This specific ansatz has been chosen due to convenience; any configuration resulting from a global rotation of the above state would be equally valid, due to the preserved SU(2) symmetry of the Hamiltonian.

With this ansatz, the solution of the Hamiltonian can be reduced to that of a 1D block of length L_c for each value of two Fourier coefficients k_y and P , to be described

in detail below. To derive this, we first write the original Hamiltonian by redefining the lattice index $i \equiv (a, m, y)$, where a denotes the x -coordinate measured from the first site of the same ‘block’, m , the block number, and y , the coordinate in the y direction. With these definitions, we can expand the fermionic annihilation operators:

$$c_{i\sigma} \equiv c_{a,m,y,\sigma} = \sum_{k_y, P} c_{a,k_y,P,\sigma} e^{i(k_y y + P x_m)}. \quad (3)$$

Here, $k_y = 2\pi n/L_y$ is the usual Fourier coefficient in the y direction, and $P = 2\pi m/N_c$ is a ‘block’ Fourier coefficient in the x direction, similar to q in the spiral ansatz.

Using these definitions, the Hamiltonian can be recast:

$$\begin{aligned} \mathcal{H} = & \sum_{k_y, P, \sigma} \left\{ \sum_{a=1}^{L_c-1} (-t) (c_{a+1,k_y,P,\sigma}^\dagger c_{a,k_y,P,\sigma} + \text{h.c.}) \right. \\ & + (-t) (c_{1,k_y,P,\sigma}^\dagger c_{L_c,k_y,P,\sigma} e^{-iP} + \text{h.c.}) \\ & - \sum_a (2t \cos(k_y) + \mu) c_{a,k_y,P,\sigma}^\dagger c_{a,k_y,P,\sigma} \left. \right\} \\ & - J_H \sum_{a,k_y,P} \{ c_{a,k_y,P,\uparrow}^\dagger c_{a,k_y,P+q,\downarrow} + \text{h.c.} \}. \end{aligned} \quad (4)$$

For any Fourier mode (k_y, P) , the above Hamiltonian is equivalent to a 1D tight-binding Hamiltonian of a block of length L_c , at an effective chemical potential $\mu(k_y) = -2t \cos(k_y) - \mu$. The Hund's term mixes the P, \uparrow state for each site a with the corresponding $P + q, \downarrow$ state.

Each solution provides $2L_c$ eigenvalues $\lambda_{k_y,P,n}^q$, where $n \in [0, 2L_c]$, and the ground state energy is given by $E(q) = \sum_{k_y,P,n} \lambda_{k_y,P,n}^q (1 - \theta(\lambda_{k_y,P,n}^q))$, where $\theta(x)$ is the usual Heaviside theta function. To find the optimum value $q = q^*$ for any given set of parameters, we calculate $E(q)$ for all allowed values of q and find the minimum. We solve these equations for various values of μ, J_H, L_0, L_1 and L_y to gain insight into the effect of the RKKY interaction on the ground state order.

To investigate the transport properties, and explore parallels with the GMR systems, we calculate the Drude weight, which is an indicator of the DC conductivity. In linear response, the Drude weight D is determined by the current-current correlation function Λ_{xx} by [45]

$$\frac{D}{\pi e^2} = \langle -k_x \rangle - \text{Re } \Lambda_{xx}(q = 0, \omega \rightarrow 0). \quad (5)$$

Here, $\langle -k_x \rangle$ denotes the kinetic energy along the x direction in the system, and $\Lambda_{xx}(q = 0, \omega \rightarrow 0)$ is the Fourier transform of the current-current correlation function $\Lambda_{xx}(i - j, \tau - \tau') \propto \langle J_x(i, \tau) J_x(j, \tau') \rangle$, where J_x is the current operator in the x -direction given by $J_x = (-it) \sum_{i,\sigma} (c_{i+x,\sigma}^\dagger c_{i,\sigma} - \text{h.c.})$. The current-current correlation function can be calculated in a straightforward manner since it is quadratic in the fermions, and further simplified using the Fourier components (k, P) as in the case of the Hamiltonian (see Appendix B for details).

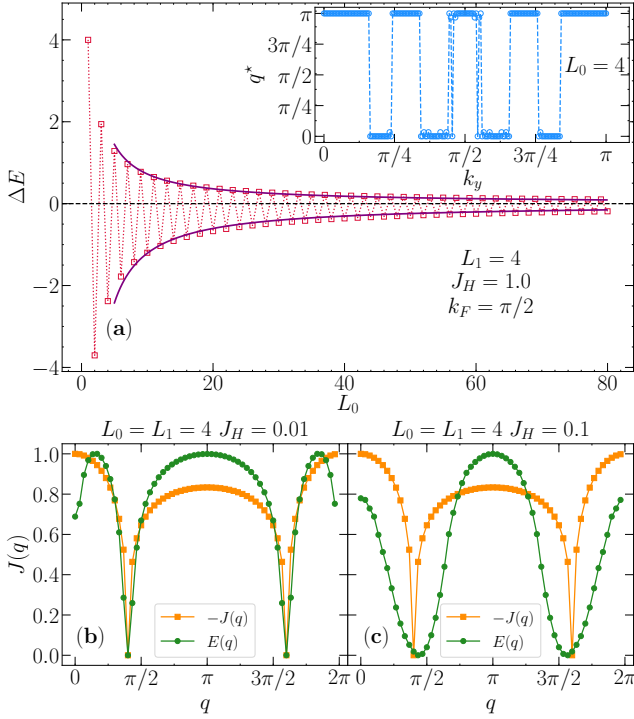


FIG. 2. (a) Energy difference ΔE between AF and FM states with increasing L_0 , at $k_F = \pi/2$; $L_1 = 4$ and $J_H = 1$. The period of oscillation is 2, and the envelope goes as $1/L_0$, consistent with the RKKY form $\sim \cos(2k_F r)/r = \cos(\pi L_0)/L_0$. Inset shows that the optimum $q = q^*$ value flips between FM and AF with changing chemical potential μ for the same parameters, fixing $L_0 = 4$. (b) and (c) show the dispersion $E(q)$ (green circles, scaled) for $J_H = 0.01$ and 0.1 at $k_F = \pi/10$. SP order at small J_H gradually evolves towards FM/AF with increasing J_H . Orange squares show results from second order perturbation for small J_H (also scaled). In second order, $\delta E_2(q) = -\sum_{m,m'} J_{m,m'} \vec{S}_m(q) \cdot \vec{S}_{m'}(q) = -\text{Re}(J(q))$ (see Appendix A for details), whose minimum coincides with that of $-\text{Re}(J(q))$, as the plots demonstrate.

This provides us with the crucial tool to explicitly calculate and connect the transport with the ground state properties, constituting an advance over previous theoretical work [46].

III. RESULTS

We now present results on the ground states for various parameter values. As seen in Eq. 4, the system is effectively a sum of 1D superlattices with an effective chemical potential $\mu(k_y)$ corresponding to each transverse mode k_y . To gain more insight, we start by considering the 1D case alone. This will form the basis for understanding the case of wide superlattices. In what follows, the energy scale is set by $t = 1$. A majority of the results will be presented for $J_H = 1$. Using detailed phase diagrams, we will later demonstrate that the system properties are

remarkably similar over a large range of J_H values about this point.

A. 1D superlattices

Figure 2 summarizes our results on one-dimensional superlattices for different parameter values. We start by demonstrating the effect of the spatially varying RKKY interaction in our system in Fig. 2(a), by showing how the lowest energy state oscillates between FM and AF configurations with changing buffer length L_0 at half filling [$\mu(k_y) = 0$; we denote μ as a function of ‘ k_y ’ to remind us of the connection with our original quasi-1D system], in a typical superlattice with $L_1 = 4$. If we define a nominal k_F by $-2t \cos(k_F) = -\mu(k_y)$, then we have $k_F = k_y = \pi/2$. The period of oscillations and the envelopes of the $\Delta E \equiv E_{\text{FM}} - E_{\text{AF}}$ curve are in agreement with the RKKY form $\sim \cos(2k_F r)/r$. Here, as explained earlier, the distance r between the magnetic ‘impurities’ of the original interaction is set by the buffer size L_0 separating the L_1 -sized magnetic regions. The inset shows the optimum values q^* for different μ at $J_H = 1$ and $L_0 = 4$. We find that at this value of J_H , the ground state is FM or AF for most of the μ values, and SP phases are largely suppressed.

On the other hand, Figs. 2(b) and 2(c) show the dispersion relations $E(q)$ for smaller values of $J_H = 0.01$ and 0.1 , respectively, for $k_F = \pi/10$. As an independent check on our calculations, we also compare these with the results from a second order perturbation expansion for small J_H (see figure caption and Appendix A for details). We find that at $J_H = 0.01$, the optimum q is spiral, and as expected, perturbation theory works well. As J_H is increased, the optimum q tends to move to either FM or AF, and the agreement with perturbation results also becomes worse, as one would expect, shown by the results for $J_H = 0.1$.

B. Quasi-1D superlattices

In this subsection, we present our main results on the quasi-1D superlattice system which reduces to a collection of separate 1D systems at a range of chemical potentials $\mu(k_y) = -2t \cos(k_y) - \mu$, defined by the normal modes $k_y = 2\pi n/L_y$, with n varying from 0 to $L_y - 1$. We start by probing the effect of the width L_y on the system properties. Then, we move on to the transport properties by calculating D explicitly and analysing its correlation with the ground state spin configuration. We present detailed phase diagrams to study the ground state dependence on μ and J_H , noting how its periodicity changes with μ . Finally, we discuss this periodicity and its dependence on μ and other system parameters in detail, and provide a simple RKKY framework that, somewhat surprisingly, explains a majority of these observations.

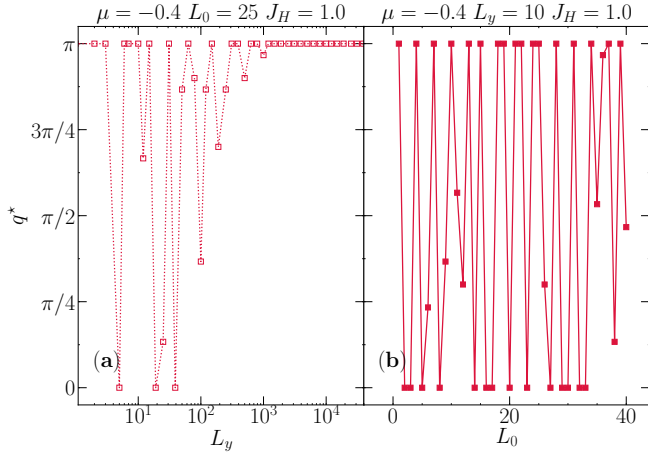


FIG. 3. (a) Optimum value q^* over L_y values $\sim [10, 10^4]$ at $\mu = -0.4$, $L_0 = 25$, $L_1 = 4$ and $J_H = 1.0$. We find that in a large range $L_y \lesssim 10^3$, the ground state consists of various SP orders, whereas for large $L_y \gtrsim 10^3$ these are suppressed and the system has an AF ground state at the chosen parameter values. (b) shows optimum $q = q^*$ vs L_0 for small $L_y = 10$, where we see rapid oscillations without any uniform periodicity (see text for more details). The number of cells N_c is kept at 60.

1. Dependence on L_y

To relate our results to the GMR experiments better, where the transverse dimensions are orders of magnitude larger than the lengths L_0 and L_1 , we explore our system over a large range of values of $L_y \in [\mathcal{O}(10), \mathcal{O}(10^4)]$, while keeping $L_0, L_1 \sim \mathcal{O}(10)$. Figure 3 summarizes these results in a nutshell. Figure 3(a) shows the optimum $q = q^*$ for different values of L_y up to 10^4 , for fixed μ, L_0, L_1 and J_H . We find that over a large range $L_y \lesssim 10^3$, the system consists of a variety of SP orders until $L_y \gtrsim \mathcal{O}(10^3)$, where they are suppressed and the ground state displays AF order at our parameter values. We emphasize that this is the result of a sum over all transverse modes k , and depends intricately on the energy balance of the various orders at each $\mu(k)$ [see Eq.(4)].

In comparison, we further report in Fig. 3(b) a representative plot of the optimal $q = q^*$ for a small fixed $L_y \sim \mathcal{O}(10)$ but with varying buffer size L_0 , at the same μ and J_H values. We find that the system shows rapid oscillations between FM and AF with intermediate SP states, but there is no clear periodicity in their variation. We will discuss this effect and contrast it with the behavior at large L_y in detail below.

2. Transport properties

Having demonstrated that the SP phases are suppressed when $L_y \gg L_0, L_1$, we consider a specific case with $L_y = 20000$, in order to investigate the influence of the magnetic ordering of the classical spins on the

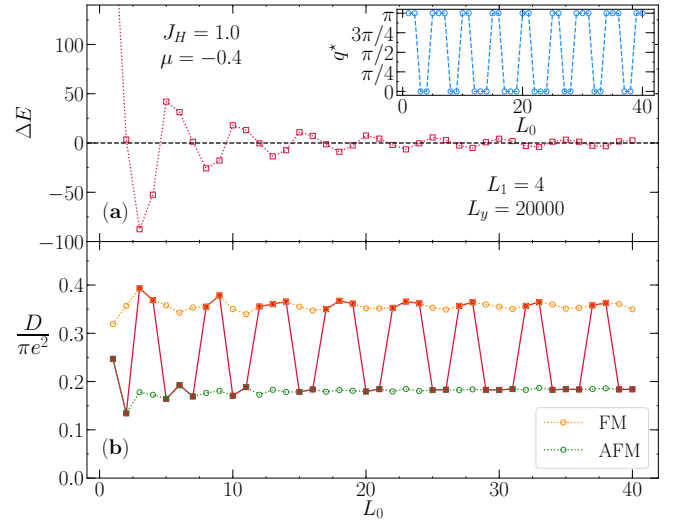


FIG. 4. (a) Energy difference ΔE between FM and AF states (main) and optimum value q^* (inset) vs L_0 for very wide superlattices ($L_y = 20000$) at $\mu = -0.4$, $J_H = 1$ and $L_1 = 4$. SP phases are suppressed in this regime, but in contrast to the results for $L_y \sim \mathcal{O}(10)$, the ground state oscillates between FM and AF with a period ~ 5 sites. $\Delta E = E_{\text{FM}} - E_{\text{AF}}$ shows corresponding oscillations with a magnitude that decays with L_0 . (b) the Drude weight D for the FM (orange) and AF (green) states for the same parameters. The FM state value is $\sim 2-3$ times larger throughout, leading to large oscillations in D (red) as the ground state keeps flipping between FM and AF. The number of cells N_c is kept at 60.

all-important transport properties of the fermions. Figure 4 summarizes our results on the ground state and the Drude weight for this case, at $\mu = -0.4$ and $J_H = 1$. The inset in Fig. 4(a) shows that in contrast to the behavior at small L_y , the system at large L_y oscillates periodically between FM and AF states with a period ~ 5 lattice sites. In the main plot, Fig. 4(a), the energy difference $\Delta E = E_{\text{FM}} - E_{\text{AF}}$ is plotted against L_0 . The curve oscillates between positive and negative values as the ground state changes from AF to FM respectively. The magnitude of the oscillation decays with increasing L_0 , in keeping with the intuitive expectation that the RKKY interaction should fall off with increasing distance between the magnetic blocks.

Figure 4(b) shows the corresponding results for the Drude weight D for both the FM and AF states. We find that the conductivity in the FM state is consistently 2–3 times higher than the AF state throughout the whole L_0 range. As a result, the actual D shows robust, large oscillations in response to the periodic shifts in the ground state order. The amplitude of the oscillations appears to remain approximately constant throughout the whole L_0 range in the plot. However, as we will elaborate in the Discussion section (Sec. IV) below, this is an artifact of being confined to $T = 0$. At any finite temperature, we should expect a gradual suppression with increasing L_0 .

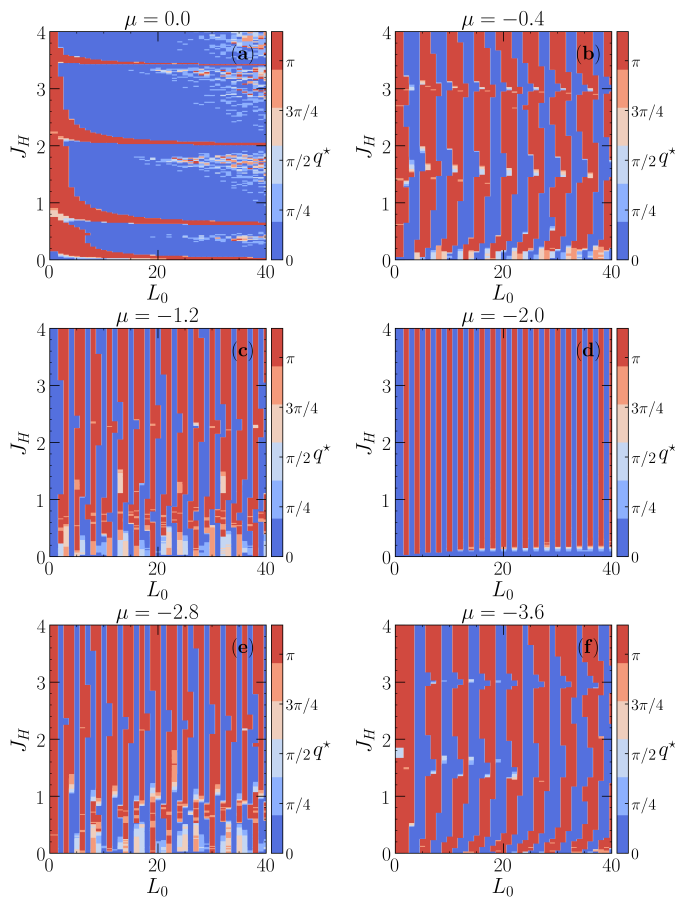


FIG. 5. Phase diagrams in $L_0 - J_H$ plane for different μ values, at $L_y = 20000$ and $L_1 = 4$. Away from half-filling ($\mu \neq 0$), the systems show periodic oscillations between FM and AF with L_0 over essentially the whole range of $J_H \lesssim 4$. The basic period is approximately constant for a given μ , but becomes smaller as it is reduced, reaching a minimum of 2 sites at $\mu = -2$, beyond which it increases again, displaying an approximate symmetry around this value. In contrast, $\mu = 0$ (and $\mu = -4$, not shown) show no periodicity, and persistent AF (FM for $\mu = -4$) regions forming narrow ‘fingers’ running across the plots (see text).

3. Phase diagrams

Having analysed the ground state and transport properties for a specific value of μ and J_H , we would like to have more insight into how the system evolves as we vary these parameters. To that end, we construct detailed phase diagrams in the $L_0 - J_H$ plane with varying μ , at large $L_y = 20000$ and $L_1 = 4$, as shown in Fig. 5. We find that away from half-filling ($\mu \neq 0$), the ground state shows periodic oscillations with L_0 for all values of μ . While the pattern changes somewhat with increasing J_H , the basic periodicity remains surprisingly constant over the whole range $J_H \lesssim 4$.

On the other hand, the periodicity shows a strong and systematic dependence on μ , reducing monotonically as

$|\mu|$ is increased until it reaches a minimum of 2 sites at $\mu = -2$, reminiscent of the results at half-filling for 1D systems, and then increasing again. The results show an intriguing approximate (but not exact) symmetry around this value, as evidenced by the similarity of the periods and patterns at, for example, $\mu = -0.4$, and its counterpart, $\mu = -3.6$. By the time the system is close to half-filling, $\mu = 0$, the period is so large that it is not discernible at the relevant length scales $L_0 \lesssim 40$. Instead, we find that the phase diagram is mostly dominated by the FM phase at moderate to large L_0 , while the AF phase dominates at small L_0 . Remarkably, at certain values of J_H , the AF phase extends across the full L_0 range, forming narrow fingers running across the plot. At $\mu = -4$ (not shown), the roles are reversed, and it is the FM phase that forms narrow fingers across the plot.

4. Analysis of periodicity

The results on the periodicity of the ground state and transport deserve further analysis. In Fig. 6(a), we summarize all the relevant information about the ground state order at large L_y and its variation with L_0 at different values of μ , L_1 and L_y (we have already established the remarkable consistency of these results over a large range of J_H values).

To begin with, we show plots of ΔE vs L_0 for three values of the chemical potential $\mu = -0.4$, -1.2 and -2.0 respectively, at $L_1 = 4$ and $L_y = 1000$. To extract the average period of oscillations, we fit these curves to a functional form $f(x) \sim a \cos(kx + b)/x^l$ (similar to the perturbative RKKY form), where a , b , k and l are fitting parameters. The resultant fits are shown by the solid lines in the plot and demonstrate that even though the oscillations are, in general, complex and not simple cosines by any means (see the $\mu = -1.2$ plot for example), the basic periodicity, as well as the decaying envelope of the amplitude, can be fit remarkably well by such a simple function.

In addition, to show the dependence on L_y and L_1 , we include plots of $L_y = 20000$ (appropriately scaled by a factor of 20) and $L_1 = 10$ at $\mu = -0.4$ and -1.2 respectively. The former plot is almost identical to $L_y = 1000$ (the circles have been shifted slightly in the plot for visual clarity), demonstrating that beyond $L_y \gtrsim 1000$, there is no change in the system characteristics with further increase in L_y , beyond a trivial scaling of the energies. The $L_1 = 10$ plot, on the other hand, shows the same periodicity but a different ‘structure’ compared to $L_1 = 4$. This establishes that the finite size of the spin blocks is responsible, at least in part, for the detailed internal structure of the curves but the basic periodicity does not seem to depend on these details.

In Fig. 6 (b), the period extracted from the fitting functions (expressed in terms of an effective wavenumber, k_{eff}) is plotted against the chemical potential μ for two different L_1 values. As discussed above, the basic

periodicity is independent of L_1 , and shows a monotonic decrease from $\mu = 0$ to $\mu = -2$, after which it rises symmetrically towards $\mu = -4$. Due to the particle-hole symmetry at $\mu = 0$, the plot is, of course, symmetric about half filling.

In order to explain the periodicity, we take a cue from our previous analysis and repeat the fitting process for each independent transverse mode k_y , using the same form as before to extract the basic period. The result is shown in Fig. 7, where we plot k_{eff} as a function of k_y , for two values of L_1 . The black dashed lines plot $2k_F$, defined by $-2t \cos(k_F) = -2t \cos(k_y) - \mu$. The fit shows that the form $\Delta E \sim E_0(k_F) \cos(2k_F L_0 + \phi(k_F))/L_0$, where ϕ is a k_F dependent phase and $E_0(k_F)$ is some energy scale characterizing the electron mediated interaction at

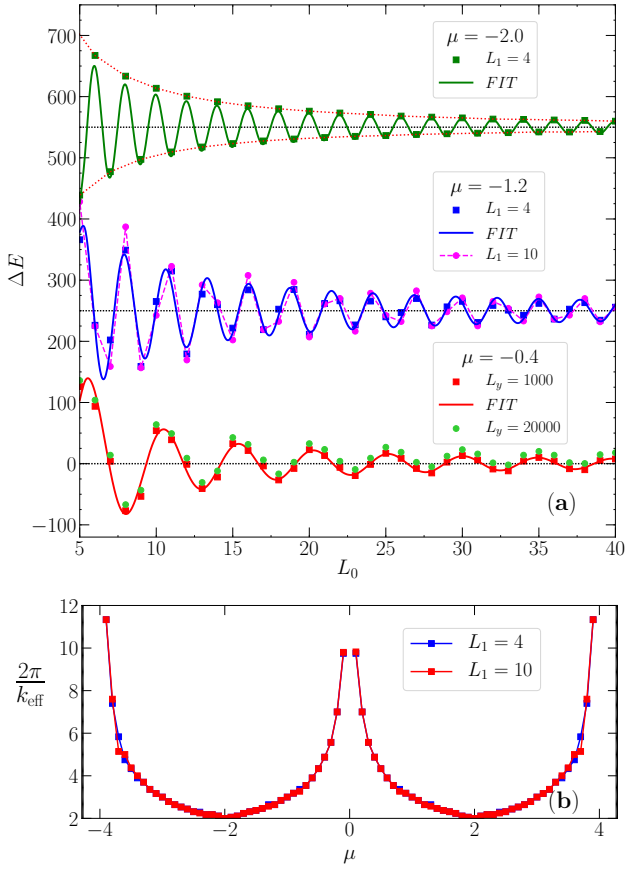


FIG. 6. (a) shows the ΔE vs L_0 plots (origins shifted for clarity, denoted by dotted black lines for each curve) at $\mu = -0.4$ (red squares), -1.2 (blue squares) and -2.0 (green squares). The solid lines of same colour show fits to the form $f(L_0) \sim a \cos(kL_0 + b)/L_0^l$. Plots of $L_y = 20000$ at $\mu = -0.4$ (green circles, scaled by factor of 20, shifted slightly for clarity) and $L_1 = 10$ at $\mu = -1.2$ (magenta circles) show that the basic period is independent of these parameters. Red dotted curves at $\mu = -2$ highlight the decaying amplitude of oscillations with increasing L_0 . (b) shows the period (expressed as $2\pi/k_{\text{eff}}$) extracted from the fits as a function of μ . The number of cells $N_c = 60$.

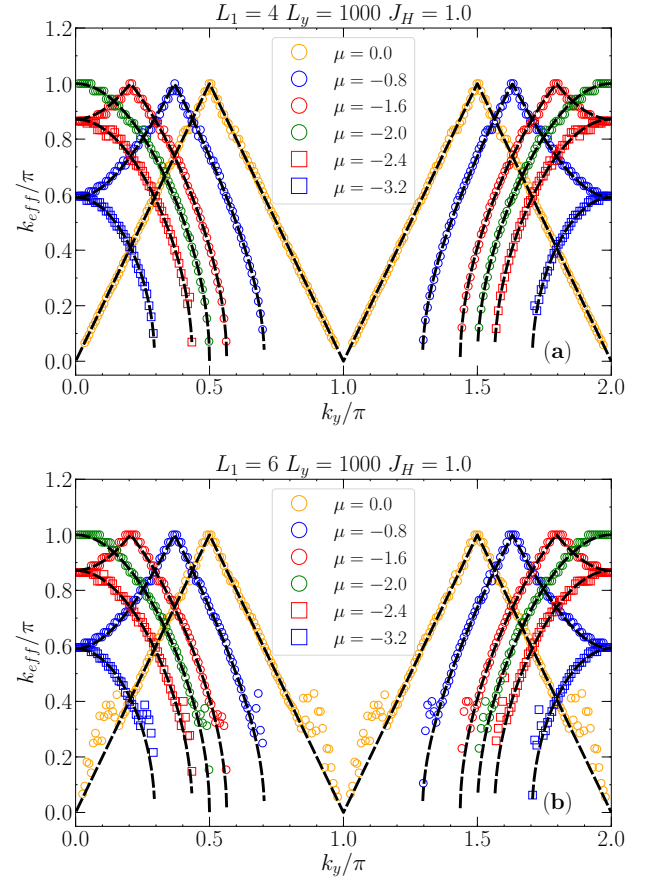


FIG. 7. The fitting wavevector k_{eff} as a function of k_y for $L_1 = 4$ and 6 , $L_y = 1000$ and $J_H = 1$ for different values of μ . ‘Conjugate’ pairs, symmetrically located around $\mu = -2$ (see text), have the same colour but different symbols (circles and squares). Black lines show $2k_F$, where k_F is defined by the usual relation $k_F = \cos^{-1}[\cos(k_y) + \mu/2]$. The close fit shows that the RKKY form using the standard Fermi vector k_F for the buffer regions is valid for $\Delta E = E_{\text{FM}} - E_{\text{AF}}$ even outside the perturbative regime for J_H . The slight deviations for $L_1 = 6$ stem from the fitting function algorithm (fitting errors are not plotted for clarity), and is not indicative of a sudden change in the periodicity of the system. Effective period of the quasi-1D system seems to be dominated by the $k_y = 0$ value.

the Fermi energy (but not necessarily of the perturbative RKKY form), works well for all k_y modes in our system, even though we are well outside the validity of perturbation theory (as seen in the 1D case discussed earlier).

The total ΔE of the quasi-1D system is given by the sum of the individual terms for each mode k_y , weighed by the functions $E_0(k_F)$. Nevertheless, it seems that away from half filling, the total periodicity is dominated by the value at $k_y = 0$, i.e., $\cos^{-1}(1 - |\mu|/2)$. A look at the plots reveals that the curves flatten out near this point, and their derivatives go to zero. Hence, as long as $E_0(k_F)$ and $\phi(k_F)$ are ‘reasonably’ flat functions of k_F , the sum will be dominated by terms around $k_y = 0$, whereas the

rest of the terms will be cancelled quickly due to fast fluctuations in their phases. In contrast, at $\mu = 0$, the plot is a straight line, and the sum over k_y leads to a flat result without any periodicity in the regime $L_0 \ll L_y$. This observation immediately explains the approximate symmetry around $\mu = -2$, as the periods of two systems with $\mu = -2 - x$ and $\mu = -2 + x$ are the same at $k_y = 0$, as confirmed by the plots. On the other hand, since the rest of the curves are very different, this symmetry is only approximate.

These observations also provide an intuitive explanation for the contrasting behaviour of the system at small and large L_y , especially the absence of SP order in the latter regime. Since the overall periodicity at large L_y is dominated by a single mode at $k_y = 0$, where the system consists of spins \vec{S}_i that are oriented identically along the transverse dimension, it is natural to interpret the system in terms of an effective 1D superlattice model, where the long transverse chain of spins is replaced by a single, large, ‘macro-spin’, or equivalently, an enhanced J_H . However, as discussed in Section III.A, a large J_H generically tends to suppress SP phases; thereby, either ferromagnetic or antiferromagnetic orderings are more prevalent in that regime. Of course, the precise details of how this works in finite systems, with all the competing energy scales at play, are only obtained by numerical means, as our work clearly demonstrates.

While these arguments provide a basic understanding of several aspects of the results related to the periodicity and ordering in the system, more involved observations, such as the presence of sharp, horizontal ‘fingers’ at $\mu = 0$, cannot be explained by this rudimentary approach.

IV. DISCUSSION AND ANALOGY WITH EXPERIMENTS

In this section we discuss several implications of our results and compare with experimental observations.

A. Mechanism of Transport

The standard explanation for the phenomenon of GMR states that the scattering rate of one spin species is different depending on whether the spin blocks are aligned ferromagnetically or antiferromagnetically. An effective resistor model based on this can be used to explicitly show that the FM state has a lower resistivity than the AF state [36].

Since we calculate the transport from first principles using our model, our results include all the myriad quantum effects stemming from the finite sizes of L_0 , L_1 , the effect of the transverse modes k_y , the spin splitting due to a large, finite J_H , and so on, that the heuristic explanation above does not encompass. Figure 8 explains this in detail. Figs. 8(a) and 8(b) show the spin resolved Drude weight D_σ (See Appendix B), as a function of μ for fixed

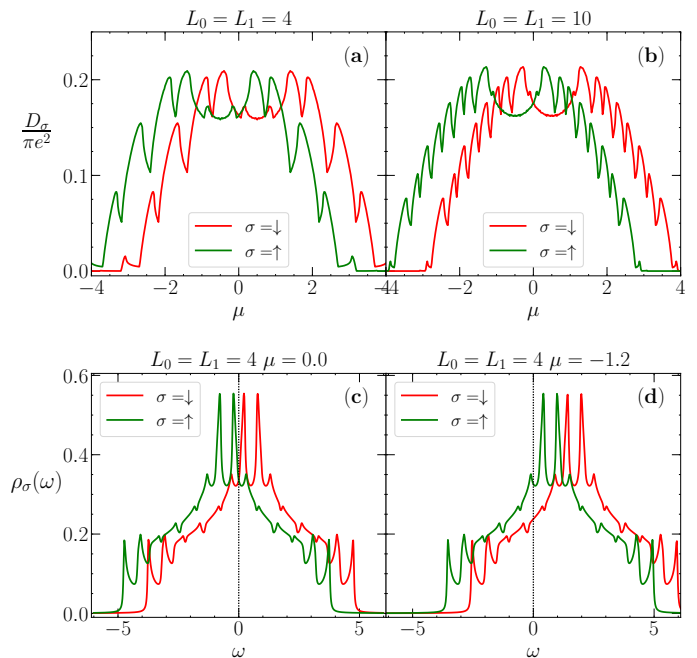


FIG. 8. Spin resolved Drude weight D_σ as a function of μ for $L_0 = L_1 = 4$ (a), and $L_0 = L_1 = 10$ (b), for an FM state, demonstrating finite size oscillations and a concave central feature of width $\simeq J_H$ in both spin channels, leading to higher value of D for the down channel in this range. Bottom plots show spin resolved density of states (DOS) $\rho_\sigma(\omega)$ at $\mu = 0$ (c) and $\mu = -1.2$ (d), demonstrating (i) only superficial resemblance with transport due to strong renormalization by current matrix elements in the transport formula (Appendix B), (ii) a mirror symmetry at $\mu = 0$ (left) leading to same transport in both spin channels, which is no longer present away from half filling (right) (see text for more details).

values of L_y and J_H , and two different combinations of L_0 and L_1 , for a FM ground state (the AF ground state has the same transport in both spin channels from symmetry considerations). Figure 8(c) plots the spin resolved density of states (DOS) for comparison. The Drude weights show marked oscillations with μ , that become finer as L_0 , L_1 are increased (top right), indicating finite size effects. The finite J_H results in a pronounced feature near $\mu = 0$ of width $\sim J_H$ in both spin curves. A consequence of this is the highly non-intuitive result that, for $\mu < 0$, the down spin has a lower resistivity in this regime compared to the up spin. This is a striking example of non-trivial physics due to the combined effect of finite size and a large, finite J_H , well beyond the scope of perturbative RKKY and scattering approaches. Outside this central region, however, the up spin has the lower resistivity, as expected. A quick look at Appendix B reveals that the transport depends on the DOS as well as the matrix elements $J_{\alpha\beta}^x$, and the latter could affect the results strongly. A comparison with the DOS plots in the lower left panel confirms this, where we find a rudimentary similarity in the oscillations, but the relative strengths are very different due to the current matrix elements.

The DOS plots [Figs. 8(c) and (d)] also highlight another aspect that impacts the transport properties. Due to the particle-hole symmetry in the system at half-filling, the total density of states is always symmetric about $E = 0$ (See Appendix C). In particular, for the FM state, where the up and down spins are well defined, this implies that the spin-resolved density of states, $\rho_{\uparrow}(E)$ and $\rho_{\downarrow}(E)$, are related by $\rho_{\uparrow}(E) = \rho_{\downarrow}(-E)$ (as seen in the lower left panel). Hence, there is a mirror symmetry in the transitions from filled to empty states in the current matrix element in Eq. (B3), and as a result, the conductivity for both spins is identical. Thus, at half-filling the increased conductivity in the FM state has a different origin compared to the standard mechanism. Away from half-filling (bottom right), this symmetry is no longer present, and the transport can be different for both spin species, as we have seen before.

This discussion reiterates how our spin-fermion Hamiltonian can capture physical effects in transport related to the geometry, filling, hopping and Hund's coupling that are absent in the standard explanations based on perturbation theory or scattering approaches.

B. Extension to finite T

One of the main constraints in our study is the restriction to $T = 0$, which ignores the effects of thermal fluctuations in our system. Before moving to finite temperatures, it is important to discuss whether true long range order can exist in our quasi-1D system at $T > 0$, in the presence of effective long range RKKY interactions between the spins \vec{S}_i . The celebrated Mermin-Wagner (MW) theorem [47–49], which states that it is impossible to have true long range order in isotropic Heisenberg systems at finite temperatures in $d \leq 2$ in the thermodynamic limit, is only valid for sufficiently short-ranged interactions. The situation with long range interactions is far less clear, even though extensions to MW have been conjectured [50]. If MW retains its validity, then only quasi long range order is possible in such systems. However, for any finite system with a characteristic length L , there exists a finite temperature scale $T_c(L)$ below which the spin-spin correlation length exceeds the system size. This sets the nominal critical temperature for that system size. In subsequent discussions of finite temperature order, this interpretation will be implicit.

Ignoring finite temperatures allows us to use variational techniques to explore a large range of parameters and sizes, as we have seen in the previous sections. On the other hand, it implies that even small energy differences can become crucial in determining the ground state and lead to large changes in its properties, an effect that will be washed away readily at finite temperatures. Our spin fermion model is amenable to sophisticated techniques for probing finite T effects, including standard Monte Carlo methods [51–56]. However, the requirement of large dimensions to rule out spiral orders makes it dif-

ficult to apply them in a straightforward manner to our setup due to constraints on computational time. On the other hand, at low temperatures, one can perform a simplified statistical analysis using the spiral mode energies $E(q)$. The expectation value of any fermionic variable, such as the Drude weight D , will then be given by

$$\langle D \rangle = \frac{\sum_q D(q) \exp(-E(q)/T)}{\mathcal{Z}}.$$

An immediate consequence is that at any finite temperature, the oscillations in $\langle D \rangle$ in Fig. 4 will decay with increasing L_0 due to the diminishing energy difference ΔE , finally getting completely washed away when $\Delta E(L_0) \sim T$. Similar results will hold for all such observables.

While it may be difficult to apply Monte Carlo methods to this system directly, our Hamiltonian may be used to study other heterostructure devices exploring various magnetic configurations in their constituents, including tunnel magnetic junctions [57, 58], where the dimensions could be small enough to apply the finite temperature techniques discussed above.

C. Comparison with Experiments

Our primary result in this paper, illustrated in Fig. 4, captures the basic transport properties of GMR by exploiting the oscillatory nature of the RKKY interactions to demonstrate periodic variations in the transport with increasing buffer size, as the system flips between FM and AF states. Several experiments done on a similar geometry on magnetic-magnetic layers such as Co/Cr or Fe/Cr [39], or magnetic-nonmagnetic layers such as Co/Ru and Co/Cu [39, 40], reported oscillations in the interlayer coupling and saturation magnetoresistance with changing buffer length. The increase in magnetoresistance varied between 6% (Ru buffer) to 65% (Cu buffer). More recently, experiments on multilayer van der Waals heterostructures [58] have demonstrated giant Tunneling Magnetoresistance (TMR) of up to 19000% based on the same principle of lower resistance in FM configurations. These measurements were done at finite temperatures, and showed marked attenuation in their oscillations [39, 40], in contrast to our results. As discussed before, however, at finite T , our model would also yield similar decaying oscillations in D with increasing buffer size.

In our current work, we have explicitly neglected the effects of spin-orbit coupling in both our Hamiltonian as well as in the variational ansatz for the \vec{S}_i . In real materials, such as Co/Pt or NiFe/Pt interfaces, the spin-orbit coupling plays an important role due to the absence of inversion symmetry in the system, and results in a canted spin arrangement in the ferromagnetic material [59–61]. In order to model such systems more accurately, it is important to extend the current formalism by including

an appropriate Dzyaloshinskii-Moriya term [43, 44], an interesting direction that we intend to pursue in future work.

The large variation in magnetoresistance among the different materials indicates a correspondingly large variation in system parameters, even though the underlying principle driving GMR presumably remains the same. Our model provides a broad and thorough framework for understanding and modeling GMR physics in an array of experimental systems with varying parameters and geometries, and can capture complex physical phenomena beyond the confines of standard perturbation techniques. Possible extensions include modelling one or more specific systems in greater detail by modifying the current Hamiltonian suitably, and studying the ordering and transport in them.

V. CONCLUSIONS

In this paper, we explored the ground state and transport properties of a quasi one-dimensional spin-fermion model in a superlattice geometry. We showed that due to the extended transverse dimension and superlattice structure, our model may display FM, SP and AF ground states at different parameter values. However, when L_y is much larger than other dimensions, SP phases are suppressed, and away from half-filling, the ground state shows periodic oscillations between FM and AF states, resulting in corresponding oscillations of the transport due to higher conductivity in the FM state. Using detailed phase diagrams, we demonstrated how the oscillations varied with μ and showed that the basic RKKY form can be used to understand their periodic behavior even outside the perturbative regime. We discussed the spin resolved transport behaviour with μ , and demonstrated anomalous non-perturbative results that standard scattering theory cannot access. We compared our results to several experiments, establishing the capacity of our model to capture GMR physics comprehensively. The ability of the model to incorporate different geometries and parameter regimes far surpassing conventional perturbative approaches, and access thermal fluctuations using standard Monte Carlo simulations opens up the possibility of studying a range of modern heterostructure devices [57, 58] where GMR physics is relevant.

We thank Prof. Elbio Dagotto for useful comments. ST acknowledges discussions with Stefano Chesi. The work of RTS was supported by the grant DESC0014671 funded by the U.S. Department of Energy, Office of Science. RM acknowledges support from NSFC Grants No. U1930402, No. 11674021, 11851110757 and No. 11974039. All numerical computations were carried out on the Tianhe-2JK at the Beijing Computational Science Research Center (CSRC).

Appendix A: Derivation of Perturbation Expansion

In this section, we derive the perturbative expressions used in Fig. 2 (b) and 2(c) for the 1D system at half-filling ($\mu = 0$). When $J_H \ll t$, the exchange coupling term in Eq. (1) can be treated as a perturbation. Thus, we have

$$\begin{aligned}\mathcal{H} &= \mathcal{H}_0 + \mathcal{H}_1, \quad \text{where,} \\ \mathcal{H}_0 &= (-t) \sum_{\langle ij \rangle} (c_{i\sigma}^\dagger c_{j\sigma} + \text{h.c.}) = (-2t) \sum_{k\sigma} \cos k \, c_{k\sigma}^\dagger c_{k\sigma} \\ \mathcal{H}_1 &= J_H \sum_{i,\alpha,\beta} (\vec{S}_i \cdot \vec{\sigma}) c_{i\alpha}^\dagger c_{i\beta}.\end{aligned}\quad (\text{A1})$$

As in the main text, we assume that the spins are confined to the x - y plane for convenience, so that $\vec{S}_i = (\cos(\theta_i), \sin(\theta_i), 0)$, where θ_i is the usual polar angle between \vec{S}_i and the x -axis. Then \mathcal{H}_1 can be written as

$$\begin{aligned}\mathcal{H}_1 &= J_H \sum_{i,\alpha,\beta} (\vec{S}_i \cdot \vec{\sigma}) c_{i\alpha}^\dagger c_{i\beta} \\ &= J_H \sum_i (e^{-i\theta_i} c_{i\downarrow}^\dagger c_{i\uparrow} + \text{h.c.}) \\ &= \left(\frac{J_H}{N}\right) \sum_{i,k_1,k_2} (e^{-i\theta_i} e^{-ir_i(k_2-k_1)} c_{k_2\downarrow}^\dagger c_{k_1\uparrow} + \text{h.c.})\end{aligned}\quad (\text{A2})$$

To do the perturbation theory at $T = 0$, we define the ground state of the free electron system \mathcal{H}_0 by $|G\rangle$, and the relevant excited states corresponding to an excitation from a filled state at (k_1, σ) with $k_1 < k_F$ to an empty state $(k_2, -\sigma)$ with $k_2 > k_F$ by $|k_1\sigma, k_2 - \sigma\rangle$.

The first order correction to the energy, δE_1 , is given by

$$\delta E_1 = \langle G | \mathcal{H}_1 | G \rangle = 0, \quad (\text{A3})$$

whereas the second order correction, δE_2 , results in

$$\begin{aligned}\delta E_2 &= -\left(\frac{J_H}{N}\right)^2 \sum_{\substack{k_1 < k_F \\ k_2 > k_F}} \frac{\sum_\sigma |\langle k_1\sigma, k_2 - \sigma | \mathcal{H}_1 | G \rangle|^2}{-2t (\cos k_2 - \cos k_1)} \\ &= -\left(\frac{J_H}{N}\right)^2 \sum_{\substack{k_1 < k_F \\ k_2 > k_F}} \frac{\{|\sum_i e^{-i\theta_i} e^{-ir_i q}|^2 + |\sum_i e^{i\theta_i} e^{-ir_i q}|^2\}}{-2t (\cos k_2 - \cos k_1)} \\ &= -\left(\frac{2J_H}{N}\right)^2 \sum_{\substack{ij \\ i < j}} \left\{ \sum_{\substack{k_1 < k_F \\ k_2 > k_F}} \left(\frac{\cos(r_{ij}q) \cos\theta_{ij}}{-2t (\cos k_2 - \cos k_1)} \right) \right\} \\ &= -\left(\frac{2J_H}{N}\right)^2 \sum_{\substack{ij \\ i < j}} \left\{ \sum_{\substack{k_1 < k_F \\ k_2 > k_F}} \left(\frac{\cos(r_{ij}q) \vec{S}_i \cdot \vec{S}_j}{-2t (\cos k_2 - \cos k_1)} \right) \right\}\end{aligned}\quad (\text{A4})$$

Here, $r_{ij} = r_i - r_j$, $q = k_2 - k_1$ and $\theta_{ij} = \theta_i - \theta_j$. Thus,

the perturbative correction is

$$\delta E_2 = - \sum_{\substack{ij \\ i < j}} J_{ij} \vec{S}_i \cdot \vec{S}_j, \quad \text{where,}$$

$$J_{ij} = \left(\frac{2J_H}{N} \right)^2 \sum_{\substack{k_1 < k_F \\ k_2 > k_F}} \left(\frac{\cos(r_{ij}q)}{-2t(\cos k_2 - \cos k_1)} \right). \quad (\text{A5})$$

In the continuum limit, this double sum may be calculated approximately [25, 62] to yield

$$J(r) = \left(\frac{J_H^2 k_F^2}{4\pi \sin^2(k_F/2)} \right) \left(\frac{\cos(2k_F r)}{r} \right) \quad (\text{A6})$$

In our superlattice, we may write the total energy as

$$\delta E_2 = - \sum_{\substack{a,m \\ a',m'}} J_{am,a'm'} \vec{S}_m \cdot \vec{S}_{m'}$$

$$= \sum_{m,m'} \left(\sum_{a,a'} J_{am,a'm'} \right) \vec{S}_m \cdot \vec{S}_{m'} \quad (\text{A7})$$

Hence, the effective block-block interaction $J_{m,m'} = (\sum_{a,a'} J_{am,a'm'})$. By using translation invariance and setting the intra-block couplings $J_{am,a'm}$ to zero (since they only contribute a constant as all \vec{S}_i in one block point in the same direction), and using the ansatz for \vec{S}_m in Eq. 2, we have

$$\delta E_2 = - \sum_{m,m'} J_{mm'} \vec{S}_m \cdot \vec{S}_{m'}$$

$$= - \sum_{mm'k} J(k) e^{ik(x_m - x_{m'})} \cos(q(x_m - x_{m'}))$$

$$= -\text{Re}(J(q)). \quad (\text{A8})$$

Appendix B: Conductivity calculation

In this section, we show the details of the conductivity calculation used in the main paper, summarized by Eq.(5).

The current operator in the x-direction, J_x , is given by

$$J_x = (-it) \sum_{i,\sigma} (c_{i+x,\sigma}^\dagger c_{i,\sigma} - \text{h.c.}) \quad (\text{B1})$$

Using Eqs. (2) and (3), this can be written as

$$J_x = (-it) \sum_{k_y, P, \sigma} \left\{ \sum_{a=1}^{L_c-1} (c_{a+1, k_y, P, \sigma}^\dagger c_{a, k_y, P, \sigma} - \text{h.c.}) \right.$$

$$\left. + (c_{1, k_y, P, \sigma}^\dagger c_{L_c, k_y, P, \sigma} e^{-iP} - \text{h.c.}) \right\} \quad (\text{B2})$$

Making use of the general expression for any retarded bosonic operator [63], the expression for the current-current correlation function $\Lambda_{xx}(q=0, \omega)$ can be written as

$$\Lambda_{xx}(q=0, \omega) = \sum_{nm} \frac{|\langle n | J_x | m \rangle|^2}{\mathcal{Z}} \left(\frac{e^{-\beta E_n} - e^{-\beta E_m}}{\omega + E_n - E_m + i\delta} \right), \quad (\text{B3})$$

where m, n , are multiparticle eigenstates of the full Hamiltonian, E_m, E_n , are the corresponding eigenvalues and \mathcal{Z} is the partition function.

For a spiral ansatz of the form given by Eq. (2), the eigenvalues can be calculated by diagonalizing an effective one-dimensional Hamiltonian given by Eq. (4). This can be solved by the following transformation

$$c_{a, k_y, P, \sigma} = \sum_{\alpha} u_{\alpha, \sigma}^a(k_y, P, q) \gamma_{\alpha}(k_y, P, q). \quad (\text{B4})$$

Using this transformation, the current operator J_x can be written as

$$J_x = \sum_{\substack{\alpha\beta \\ k_y, P}} J_{\alpha\beta}^x \gamma_{\alpha}^\dagger(k_y, P, q) \gamma_{\beta}(k_y, P, q), \quad \text{where,}$$

$$J_{\alpha\beta}^x = (-it) \sum_{\sigma} \left\{ \sum_{a=1}^{L_c-1} \left(u_{\alpha\sigma}^{*a+1}(k_y, P, q) u_{\beta\sigma}^a(k_y, P, q) - \text{h.c.} \right) \right.$$

$$\left. + \left(u_{\alpha\sigma}^{*1}(k_y, P, q) u_{\beta\sigma}^{L_c}(k_y, P, q) e^{-iP} - \text{h.c.} \right) \right\}. \quad (\text{B5})$$

Using Eq. (B3) and the fact that the multiparticle states m, n are just Slater determinants of the single-particle eigenstates $|\alpha(k_y, P, q)\rangle$ (with energies ϵ_{α}), Λ_{xx} can be finally rewritten as

$$\Lambda_{xx}(q=0, \omega) = \sum_{\substack{\alpha\beta \\ k_y, P}} |J_{\alpha\beta}^x|^2 \left(\frac{f(\epsilon_{\alpha}) - f(\epsilon_{\beta})}{\omega + \epsilon_{\alpha} - \epsilon_{\beta} + i\delta} \right). \quad (\text{B6})$$

The expectation value of the kinetic energy in the x-direction, defined by $k_x = \sum_{\langle ij \rangle} \sigma (c_{i\sigma}^\dagger c_{j\sigma} + \text{h.c.})$ can be calculated in exactly the same manner as the current, and using this, the total and spin resolved (for the FM state) Drude weights are given by

$$\frac{D}{\pi e^2} = \langle -k_x \rangle - \text{Re} \Lambda_{xx}(q=0, \omega \rightarrow 0), \quad \text{and}$$

$$\frac{D_{\sigma}}{\pi e^2} = \langle -k_{x, \sigma} \rangle - \text{Re} \Lambda_{xx, \sigma}(q=0, \omega \rightarrow 0). \quad (\text{B7})$$

Appendix C: Particle-Hole symmetry

In this section, we briefly demonstrate the particle-hole symmetry of the Hamiltonian at half-filling. Using the definitions $c = (c_{1\uparrow}, \dots, c_{N\uparrow}, c_{1\downarrow}, \dots, c_{N\downarrow})^T$ and

$\bar{c} = (c_{1\uparrow}^\dagger, \dots, c_{N\uparrow}^\dagger, c_{1\downarrow}^\dagger, \dots, c_{N\downarrow}^\dagger)$, the Hamiltonian in Eq. (1) can be written compactly as $\mathcal{H} = \bar{c} H c$, where

$$H = \begin{pmatrix} \hat{\mathcal{H}}_{kin} - J_H \hat{S}^z & -J_H(\hat{S}^x - i\hat{S}^y) \\ -J_H(\hat{S}^x + i\hat{S}^y) & \hat{\mathcal{H}}_{kin} + J_H \hat{S}^z \end{pmatrix}. \quad (C1)$$

Here, $(\hat{\mathcal{H}}_{kin})_{\langle jk \rangle} = (-t)$, where $\langle jk \rangle$ denotes a nearest neighbor pair, $(\hat{S}^z)_{jk} = S_j^z \delta_{jk}$, etc.

Now, we define a particle hole transformation by the following relations

$$c = U \bar{d}, \quad \text{where,}$$

$$U = \begin{pmatrix} \hat{0} & \hat{M} \\ -\hat{M} & \hat{0} \end{pmatrix}, \quad \text{and,}$$

$$M_{jk} = (-1)^j \delta_{jk} \quad (C2)$$

We note that U is unitary (and real), and hence, $U^\dagger = U^T = U^{-1}$. Applying this to the Hamiltonian, we get

$$\begin{aligned} \mathcal{H} &= \bar{c} H c = d U^{-1} H U \bar{d} \equiv d \tilde{H} \bar{d} \\ &= \text{Tr}(\tilde{H}) - \bar{d} \tilde{H}^* d = -\bar{d} \tilde{H}^* d \end{aligned} \quad (C3)$$

If this transformation is a symmetry, then $-\bar{d} \tilde{H}^* d = \bar{d} H d$, and, hence, $U^{-1} H^* U = -H$ [64]. Now,

$$\begin{aligned} U^{-1} H^* U &= \begin{pmatrix} \hat{0} & -\hat{M} \\ \hat{M} & \hat{0} \end{pmatrix} H^* \begin{pmatrix} \hat{0} & \hat{M} \\ -\hat{M} & \hat{0} \end{pmatrix} \\ &= \begin{pmatrix} M(\hat{\mathcal{H}}_{kin} + J_H \hat{S}^z)M & M(J_H(\hat{S}^x - i\hat{S}^y)M) \\ M(J_H(\hat{S}^x + i\hat{S}^y)M) & M(\hat{\mathcal{H}}_{kin} - J_H \hat{S}^z)M \end{pmatrix} \\ &= \begin{pmatrix} -\hat{\mathcal{H}}_{kin} + J_H \hat{S}^z & J_H(\hat{S}^x - i\hat{S}^y) \\ J_H(\hat{S}^x + i\hat{S}^y) & -\hat{\mathcal{H}}_{kin} - J_H \hat{S}^z \end{pmatrix} \\ &= -H. \end{aligned} \quad (C4)$$

This proves the particle-hole symmetry of the Hamiltonian at half filling.

An immediate consequence of this symmetry is that if $|\psi\rangle$ is an eigenstate of H such that $H|\psi\rangle = E|\psi\rangle$, then $UH|\psi\rangle = EU|\psi\rangle = UHU^{-1}U|\psi\rangle = -H^*U|\psi\rangle$. Thus, we have $HU|\psi^*\rangle = (-E)U|\psi^*\rangle$, and hence, for every eigenstate $|\psi\rangle$ with an eigenvalue E , there exists an eigenstate $U|\psi^*\rangle$ with an eigenvalue $-E$, and the spectrum is symmetric about zero.

Appendix D: Behavior of $\langle n \rangle$

In this section, we show the behavior of the number density, $\langle n \rangle$ as a function of the buffer length L_0 and the chemical potential μ . Figure 9 shows the variation of the average number density $\langle n \rangle$ with the buffer length L_0 at different values of the chemical potential μ (see figure caption) for the FM and AF states. We see that when L_0 is not too small ($L_0 \gtrsim 5$), the change in density is marginal ($\lesssim 0.03$). Besides, as long as $\langle n \rangle$ is also not too small, the relative change is rather minor (for example, at $\mu = -2.0$, $\langle n \rangle$ varies roughly between 0.382 and 0.372 for $L_0 \gtrsim 5$, a relative change of only about 2.6%). Hence, our calculations are done at fixed μ , which is much simpler to implement.

Figure 10, on the other hand, shows the behavior of the spin resolved densities $\langle n_{i\sigma} \rangle$ with μ and the supercell coordinates (consisting of one spin block and one buffer region respectively) x_i for a given set of L_0 , L_1 and J_H values. Figure 10 (a) shows the variation of the total density n_σ with μ for the FM state. As expected, $\langle n_\uparrow \rangle$ is larger throughout the whole range due to a ferromagnetic J_H . In comparison, Fig. 10 (b) shows how the local density, $\langle n_{i,\sigma} \rangle$ varies with μ at the centre of the magnetic and the buffer blocks (denoted by S and B in the plots) respectively, for the same FM state. Again, as expected, $\langle n_{i,\uparrow} \rangle$ is consistently higher in S (the split is actually bigger here since the total $\langle n_\sigma \rangle$ is the average of the densities

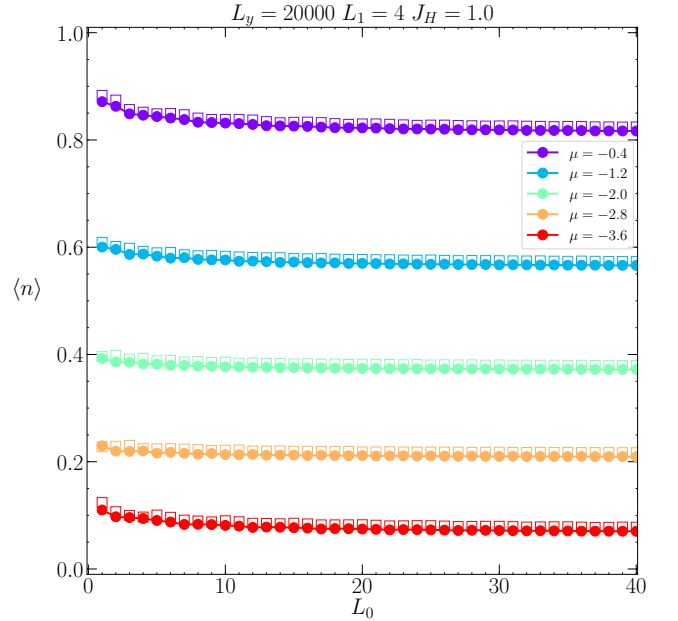


FIG. 9. The number density $\langle n \rangle$ for the FM state (filled circles) and the AF state (hollow squares of same color, shifted slightly for visual clarity) as a function of L_0 at $\mu = -0.4, -1.2, -2.0, -2.8$ and -3.6 respectively. It is clear that the variation is marginal ($\lesssim 0.03$) for $L_0 \gtrsim 5$. As a result, we choose to do our calculations keeping μ constant instead of $\langle n \rangle$.

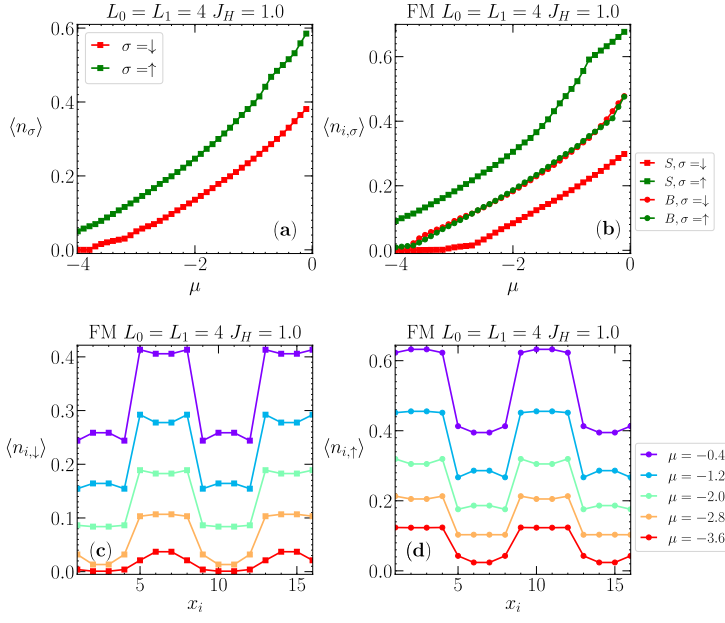


FIG. 10. The number density $\langle n_\sigma \rangle$ for the FM state as a function of μ and superlattice co-ordinate x_i . (a) plots the total density $\langle n_\sigma \rangle$ vs. μ , where $\langle n_{i,\uparrow} \rangle > \langle n_{i,\downarrow} \rangle$ throughout, as expected. (b) shows $\langle n_{i,\sigma} \rangle$ at the center of the magnetic (S) and buffer (B) blocks where we find that the polarization in the density is largely limited to the S blocks themselves. (c) and (d) show the variation of $\langle n_{i,\downarrow} \rangle$ and $\langle n_{i,\uparrow} \rangle$ respectively with the superblock co-ordinate x_i for two superblocks, with expected oscillations between S and B blocks. Even here, the effect is almost local.

in S and B). The densities in the B region, in contrast, are basically identical to each other, demonstrating that the polarization caused by J_H is largely local.

In Figs. 10 (c) and (d), we plot $\langle n_{i,\downarrow} \rangle$ and $\langle n_{i,\uparrow} \rangle$ as a function of the supercell coordinates x_i for two supercells (for the given parameters $L_0 = L_1 = 4$ that means there are 16 sites in total). As expected, $\langle n_{i,\uparrow} \rangle$ ($\langle n_{i,\downarrow} \rangle$) is larger (smaller) in the S blocks, while they are essentially the same in the B blocks. As before, we see that the oscillations between S and B are predominately local.

-
- [1] M. B. Salamon and M. Jaime, The physics of manganites: Structure and transport, *Rev. Mod. Phys.* **73**, 583 (2001).
 - [2] P. A. Lee, N. Nagaosa, and X.-G. Wen, Doping a Mott insulator: Physics of high-temperature superconductivity, *Rev. Mod. Phys.* **78**, 17 (2006).
 - [3] C. Buhler, S. Yunoki, and A. Moreo, Magnetic domains and stripes in a spin-fermion model for cuprates, *Phys. Rev. Lett.* **84**, 2690 (2000).
 - [4] S. Johnston, A. Mukherjee, I. Elfimov, M. Berciu, and G. A. Sawatzky, Charge disproportionation without charge transfer in the rare-earth-element nickelates as a possible mechanism for the metal-insulator transition, *Phys. Rev. Lett.* **112**, 106404 (2014).
 - [5] H. Park, A. J. Millis, and C. A. Marianetti, Site-selective Mott transition in rare-earth-element nickelates, *Phys. Rev. Lett.* **109**, 156402 (2012).
 - [6] W.-G. Yin, C.-C. Lee, and W. Ku, Unified picture for magnetic correlations in iron-based superconductors, *Phys. Rev. Lett.* **105**, 107004 (2010).
 - [7] W. Lv, F. Krüger, and P. Phillips, Orbital ordering and unfrustrated $(\pi, 0)$ magnetism from degenerate double exchange in the iron pnictides, *Phys. Rev. B* **82**, 045125 (2010).
 - [8] S. Liang, A. Moreo, and E. Dagotto, Nematic state of pnictides stabilized by interplay between spin, orbital, and lattice degrees of freedom, *Phys. Rev. Lett.* **111**, 047004 (2013).
 - [9] G. R. Stewart, Heavy-fermion systems, *Rev. Mod. Phys.* **56**, 755 (1984).
 - [10] P. Coleman, Heavy Fermions and the Kondo Lattice: a 21st Century Perspective (2015), [arXiv:1509.05769 \[cond-mat.str-el\]](#).
 - [11] H. Ohno, H. Munekata, T. Penney, S. von Molnár, and L. L. Chang, Magnetotransport properties of p-type (In,Mn)As diluted magnetic III-V semiconductors, *Phys. Rev. Lett.* **68**, 2664 (1992).
 - [12] H. Ohno, Making nonmagnetic semiconductors ferromagnetic, *Science* **281**, 951 (1998).
 - [13] T. Dietl, A. Haury, and Y. Merle d'Aubigné, Free carrier-induced ferromagnetism in structures of diluted magnetic semiconductors, *Phys. Rev. B* **55**, R3347 (1997).
 - [14] J. König, H.-H. Lin, and A. H. MacDonald, Theory of diluted magnetic semiconductor ferromagnetism, *Phys. Rev. Lett.* **84**, 5628 (2000).
 - [15] E. Dagotto, T. Hotta, and A. Moreo, Colossal magnetoresistant materials: the key role of phase separation, *Phys. Rep.* **344**, 1 (2001).
 - [16] O. Erten, O. N. Meetei, A. Mukherjee, M. Randeria, N. Trivedi, and P. Woodward, Theory of half-metallic ferrimagnetism in double perovskites, *Phys. Rev. Lett.* **107**, 257201 (2011).
 - [17] P. Sanyal and P. Majumdar, Magnetic model for the

- ordered double perovskites, *Phys. Rev. B* **80**, 054411 (2009).
- [18] O. N. Meetei, O. Erten, A. Mukherjee, M. Randeria, N. Trivedi, and P. Woodward, Theory of half-metallic double perovskites. I. double exchange mechanism, *Phys. Rev. B* **87**, 165104 (2013).
- [19] C. Zener, Interaction between the d -Shells in the Transition Metals. II. Ferromagnetic Compounds of Manganese with Perovskite Structure, *Phys. Rev.* **82**, 403 (1951).
- [20] P. G. de Gennes, Effects of double exchange in magnetic crystals, *Phys. Rev.* **118**, 141 (1960).
- [21] M. M. Vazifeh and M. Franz, Self-organized topological state with Majorana fermions, *Phys. Rev. Lett.* **111**, 206802 (2013).
- [22] I. Reis, D. J. J. Marchand, and M. Franz, Self-organized topological state in a magnetic chain on the surface of a superconductor, *Phys. Rev. B* **90**, 085124 (2014).
- [23] B. Braunecker and P. Simon, Interplay between classical magnetic moments and superconductivity in quantum one-dimensional conductors: Toward a self-sustained topological Majorana phase, *Phys. Rev. Lett.* **111**, 147202 (2013).
- [24] J. Klinovaja, P. Stano, A. Yazdani, and D. Loss, Topological superconductivity and Majorana fermions in RKKY systems, *Phys. Rev. Lett.* **111**, 186805 (2013).
- [25] M. A. Ruderman and C. Kittel, Indirect exchange coupling of nuclear magnetic moments by conduction electrons, *Phys. Rev.* **96**, 99 (1954).
- [26] T. Kasuya, A theory of metallic ferro- and antiferromagnetism on Zener's model, *Prog. Theor. Phys.* **16**, 45 (1956).
- [27] K. Yosida, Magnetic properties of Cu-Mn alloys, *Phys. Rev.* **106**, 893 (1957).
- [28] In this paper, we use the term RKKY to denote the conduction electron mediated spin-spin interaction in all parameter regimes, and not just in the perturbative limit.
- [29] W. Hu, R. T. Scalettar, and R. R. P. Singh, Interplay of magnetic order, pairing, and phase separation in a one-dimensional spin-fermion model, *Phys. Rev. B* **92**, 115133 (2015).
- [30] B. Braunecker, P. Simon, and D. Loss, Nuclear Magnetism and Electronic Order in ^{13}C Nanotubes, *Phys. Rev. Lett.* **102**, 116403 (2009).
- [31] B. Braunecker, P. Simon, and D. Loss, Nuclear magnetism and electron order in interacting one-dimensional conductors, *Phys. Rev. B* **80**, 165119 (2009).
- [32] M. Azhar and M. Mostovoy, Incommensurate spiral order from double-exchange interactions, *Phys. Rev. Lett.* **118**, 027203 (2017).
- [33] M. N. Baibich, J. M. Broto, A. Fert, F. N. Van Dau, F. Petroff, P. Etienne, G. Creuzet, A. Friederich, and J. Chazelas, Giant magnetoresistance of (001)Fe/(001)Cr magnetic superlattices, *Phys. Rev. Lett.* **61**, 2472 (1988).
- [34] G. Binasch, P. Grünberg, F. Saurenbach, and W. Zinn, Enhanced magnetoresistance in layered magnetic structures with antiferromagnetic interlayer exchange, *Phys. Rev. B* **39**, 4828 (1989).
- [35] P. A. Grünberg, Nobel lecture: From spin waves to giant magnetoresistance and beyond, *Rev. Mod. Phys.* **80**, 1531 (2008).
- [36] The Nobel prize in Physics 2007 - Advanced Information, [Nobel Media AB](#).
- [37] R. Skomski, RKKY interactions between nanomagnets of arbitrary shape, *Europhys. Lett.* **48**, 455 (1999).
- [38] J. Hermenau, S. Brinker, M. Marciani, M. Steinbrecher, M. dos Santos Dias, R. Wiesendanger, S. Lounis, and J. Wiebe, Stabilizing spin systems via symmetrically tailored RKKY interactions, *Nat. Comm.* **10**, 2565 (2019).
- [39] S. S. P. Parkin, R. Bhadra, and K. P. Roche, Oscillatory magnetic exchange coupling through thin copper layers, *Phys. Rev. Lett.* **66**, 2152 (1991).
- [40] S. S. P. Parkin, N. More, and K. P. Roche, Oscillations in exchange coupling and magnetoresistance in metallic superlattice structures: Co/Ru, Co/Cr, and Fe/Cr, *Phys. Rev. Lett.* **64**, 2304 (1990).
- [41] P. Fazekas, *Lecture Notes on Electron Correlation and Magnetism* (World Scientific, 1999).
- [42] E. Müller-Hartmann and E. Dagotto, Electronic Hamiltonian for transition-metal oxide compounds, *Phys. Rev. B* **54**, R6819 (1996).
- [43] T. Moriya, Anisotropic superexchange interaction and weak ferromagnetism, *Phys. Rev.* **120**, 91 (1960).
- [44] I. Dzyaloshinsky, A thermodynamic theory of weak ferromagnetism of antiferromagnetics, *J. of Phys. Chem. Solids* **4**, 241 (1958).
- [45] D. J. Scalapino, S. R. White, and S. Zhang, Insulator, metal, or superconductor: The criteria, *Phys. Rev. B* **47**, 7995 (1993).
- [46] D. M. Edwards, J. Mathon, R. B. Muniz, and M. S. Phan, Oscillations of the exchange in magnetic multilayers as an analog of de Haas-van Alphen effect, *Phys. Rev. Lett.* **67**, 493 (1991).
- [47] P. C. Hohenberg, Existence of long-range order in one and two dimensions, *Phys. Rev.* **158**, 383 (1967).
- [48] N. D. Mermin and H. Wagner, Absence of ferromagnetism or antiferromagnetism in one- or two-dimensional isotropic Heisenberg models, *Phys. Rev. Lett.* **17**, 1133 (1966).
- [49] S. Coleman, There are no Goldstone bosons in two dimensions, *Commun. Math. Phys.* **31**, 259 (1973).
- [50] P. Bruno, Absence of spontaneous magnetic order at nonzero temperature in one- and two-dimensional Heisenberg and XY systems with long-range interactions, *Phys. Rev. Lett.* **87**, 137203 (2001).
- [51] S. Yunoki, J. Hu, A. L. Malvezzi, A. Moreo, N. Furukawa, and E. Dagotto, Phase separation in electronic models for manganites, *Phys. Rev. Lett.* **80**, 845 (1998).
- [52] M. Mayr, G. Alvarez, C. Sen, and E. Dagotto, Phase fluctuations in strongly coupled d -wave superconductors, *Phys. Rev. Lett.* **94**, 217001 (2005).
- [53] G. Alvarez, C. Sen, N. Furukawa, Y. Motome, and E. Dagotto, The truncated polynomial expansion Monte Carlo method for fermion systems coupled to classical fields: a model independent implementation, *Comput. Phys. Commun.* **168**, 32 (2005).
- [54] A. Weiße, Green-Function-Based Monte Carlo Method for Classical Fields Coupled to Fermions, *Phys. Rev. Lett.* **102**, 150604 (2009).
- [55] K. Barros and Y. Kato, Efficient Langevin simulation of coupled classical fields and fermions, *Phys. Rev. B* **88**, 235101 (2013).
- [56] R. Mondaini, T. Paiva, and R. T. Scalettar, Magnetic and metal-insulator transitions in coupled spin-fermion systems, *Phys. Rev. B* **90**, 144418 (2014).
- [57] R. K. Dumas, P. K. Greene, D. A. Gilbert, L. Ye, C. Zha, J. Åkerman, and K. Liu, Accessing different spin-disordered states using first-order reversal curves, *Phys. Rev. B* **90**, 104410 (2014).

- [58] T. Song, X. Cai, M. W.-Y. Tu, X. Zhang, B. Huang, N. P. Wilson, K. L. Seyler, L. Zhu, T. Taniguchi, K. Watanabe, M. A. McGuire, D. H. Cobden, D. Xiao, W. Yao, and X. Xu, Giant tunneling magnetoresistance in spin-filter van der Waals heterostructures, *Science* **360**, 1214 (2018).
- [59] H. Yang, A. Thiaville, S. Rohart, A. Fert, and M. Chshiev, Anatomy of Dzyaloshinskii-Moriya interaction at Co/Pt Interfaces, *Phys. Rev. Lett.* **115**, 267210 (2015).
- [60] R. M. Rowan-Robinson, A. A. Stashkevich, Y. Roussigné, M. Belmeguenai, S.-M. Chérif, A. Thiaville, T. P. A. Hase, A. T. Hindmarch, and D. Atkinson, The interfacial nature of proximity-induced magnetism and the Dzyaloshinskii-Moriya interaction at the Pt/Co interface, *Sci. Rep.* **7**, 16835 (2017).
- [61] H. T. Nembach, J. M. Shaw, M. Weiler, E. Jué, and T. J. Silva, Linear relation between Heisenberg exchange and interfacial Dzyaloshinskii-Moriya interaction in metal films, *Nat. Phys.* **11**, 825 (2015).
- [62] Y. Yafet, Ruderman-Kittel-Kasuya-Yosida range function of a one-dimensional free-electron gas, *Phys. Rev. B* **36**, 3948 (1987).
- [63] G. Mahan, *Many-Particle Physics*, Physics of Solids and Liquids (Springer US, 2000).
- [64] S. Ryu, A. P. Schnyder, A. Furusaki, and A. W. W. Ludwig, Topological insulators and superconductors: tenfold way and dimensional hierarchy, *New J. Phys.* **12**, 065010 (2010).